Photometry and polarimetry of particulate surfaces and aerosol particles over a wide range of phase angles

6 AUTHORS, INCLUDING:

Yuriy Shkuratov

77 PUBLICATIONS **1,130** CITATIONS

Vadym G. Kaydash

V. N. Karazin Kharkiv National University

80 PUBLICATIONS **700** CITATIONS

Gorden Videen

The Space Science Institute

291 PUBLICATIONS **3,997** CITATIONS

H. Volten

National Institute for Public Health an…

91 PUBLICATIONS **2,218** CITATIONS

Photometry and polarimetry of particulate surfaces and aerosol particles over a wide range of phase angles

Yuriy Shkuratov[a],*, Sergey Bondarenko[a], Vadym Kaydash[a], Gorden Videen[b], Olga Muñoz[c], Hester Volten[d]

[a]*Astronomical Institute of V.N. Karazin Kharkov National University, 35 Sumskaya Street, Kharkov 61022, Ukraine*
[b]*Army Research Laboratory AMSRL-CI-EM, 2800 Powder Mill Road, Adelphi, MD 20783, USA*
[c]*Instituto de Astrofisica de Andalucia, CSIC, Camino Bajo de Huetor 50, Granada 18008, Spain*
[d]*Astronomical Institute "Anton Pannekoek", University of Amsterdam, Kruislaan 403, 1098 SJ Amsterdam, The Netherlands*

Abstract

We present results of photometric and polarimetric laboratory measurements of particulate surfaces undergoing different degrees of compression and aerosol particles at a phase angle range from 7 to 150°. Nine samples of natural materials with different albedo and particle sizes were measured in red ($\lambda = 0.63\,\mu$m) and blue ($\lambda = 0.44\,\mu$m) light using two different instruments: Kharkov's large-phase-angle photopolarimeter for measurements of surfaces and Amsterdam's polar nephelometer for particles in air. We compare phase curves for particulate surfaces with the corresponding measurements for single particles. Our measurements suggest that the maximum of positive polarization, which is observed for particulate surfaces at large phase angles, is mainly due to the contribution of single-particle scattering. We observe an increase in the polarization degree at large phase angles with increased sample compression. We have found the negative polarization at small phase angles to be strengthened sharply by surface compression. This is partially a geometric effect at slanting view (70°), which is explained via double scattering. For photometric data, we carried out a comparison between experimental data and the Hapke photometric model. The comparison of measured photometric phase-angle dependencies with the model reveals several model shortcomings. The principle shortcoming is the spectral dependence of the model parameters that should be independent of wavelength.
© 2007 Elsevier Ltd. All rights reserved.

Keywords: Polarimetry; Light-scattering; Photometry; Negative polarization; Opposition effect; Coherent backscatter

1. Introduction

Photometric and polarimetric laboratory measurements of particles in air and on a substrate (particulate surface) at large phase angles are important for the development of remote-sensing research of atmosphereless celestial bodies [1]. For instance, they allow one to estimate contributions of single and multiple scattering in the formation of the positive polarization maximum. They also provide an opportunity to verify the applicability of the classical radiative transfer theory [2,3] to calculate light scattering by particulate surfaces

like planetary regoliths. Experimental comparison of scattering properties of representative particles in air and corresponding particulate surfaces has been carried out with the equipment at Kharkov National University (for scattering measurements of surfaces), and the equipment currently located at the University of Amsterdam (for scattering measurements of particles in air) [4]. We have compared the light-scattering measurements for the range of small phase angles, 7–17°, that is common for both the Amsterdam instrument and the Kharkov small-phase-angle photometer/polarimeter. We later expanded the range of phase angles from 7 to 60° [5] using the Kharkov large-phase-angle photometer/polarimeter at so-called standard viewing/illuminating geometry when samples were observed from the direction perpendicular to the sample surface. All these measurements allow a direct comparison of the phase curves of intensity and the linear polarization degree of particles in air and surfaces consisting of the same particles, showing that the backscatter effect of particulate surfaces is partially due to the contribution of single scattering. In addition, it was shown that the negative polarization of the surfaces is a remnant of the negative polarization
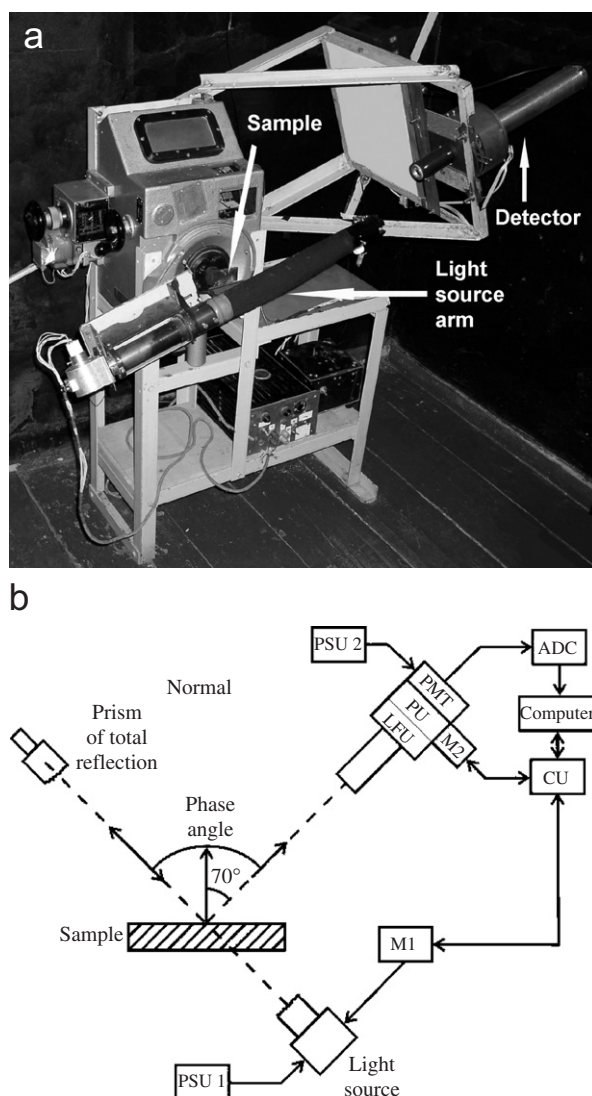

Fig. 1. A view of the Kharkov instrument at a large tilt of the receiver arm (a) and its general scheme (b). PSU–Power supply unit; M1–Phase angle motor; M2–Polarizer rotation motor; ADC–Analog-to-digital converter; CU–Control unit; PMT–Photomultiplier tube; PU–Polarizer unit; LFU–Light filters unit.

of the single scattering by the particles that constitute the surfaces. In this paper, we continue the described comparison using much wider common range of phase angles, 7–150°, with the Kharkov large-phase-angle photometer/polarimeter at tilted viewing geometry. This range includes the positive polarization maximum. In addition, we fit the results with the Hapke theory to photometric experimental data, showing some shortcomings of the model.

Table 1
The parameters of the Henyey-Greenstein scattering indicatrix for single particles calculated using weighted least-squares fit

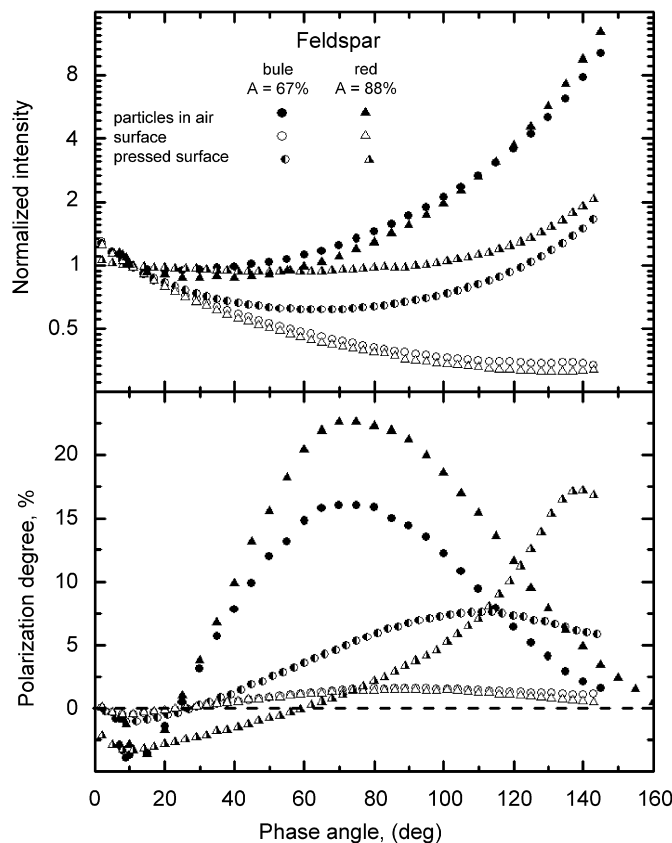| Samples	$\lambda = 0.44\,\mu m$		$\lambda = 0.63\,\mu m$	
	b	c	b	c
Olivine S	0.357	0.846	0.398	0.887
Olivine M	0.352	0.832	0.397	0.893
Locon volcano ash	0.280	0.679	0.313	0.663
Olivine L	0.309	0.776	0.355	0.785
Feldspar	0.462	0.961	0.557	0.969
Loess	0.356	0.811	0.437	0.870
Pinatubo volcano ash	0.390	0.903	0.422	0.909
Red clay	0.398	0.891	0.430	0.908
Green clay	0.472	0.937	0.479	0.942

Fig. 2. Photometric and polarimetric phase curves for particulate surfaces (compressed and uncompressed) and aerosol particles measured at $\lambda = 0.44$ and $0.63\,\mu m$ for the feldspar powder. The intensity is normalized to unity at the phase angle 10°.

2. Instruments and samples

The Kharkov instrument allows us to measure phase curves of intensity and linear polarization degree for powdered samples illuminated by unpolarized light. An image and scheme of the instrument are shown in Fig. 1a,b. In this paper, we study samples in two spectral bands with $\lambda_{eff} = 0.44$ and $0.63\,\mu m$ (the bandwidths are approximately 10%). Our polarimetric measurements have an accuracy of about 0.05%. Rotation of the arm with the light source (a lamp) can provide reliable phase-angle measurements in the range 2–$150°$ when the viewing angle is fixed at $70°$ from the surface normal (Fig. 1b). The linear dimension of the powdery samples is approximately 20 mm. The thickness of the samples is about 3–4 mm, which provides a good approximation of a semi-infinitive medium. The samples are formed with and without compacting to study the influence of surface compression on scattering properties. Albedo of the samples is determined at a phase angle of $2°$ with respect to a compressed Halon sample [6].

The measurements are made when the optical axis of the receiver containing a photomultiplier is aligned at $70°$ relatively to the normal to the sample surface (see Fig. 1a,b). The scattering plane is perpendicular to the sample surface. This oblique viewing geometry is an important point that distinguishes the measurements presented here from our previous data [4,5].

The Amsterdam light scattering instrument for measuring aerosol particles allows measurements of all 16 elements of the scattering matrix as a function of phase angle of ensembles of randomly oriented particles under single-scattering conditions in the phase angle range from 7 to $175°$. A detailed description of the instrument is given in [7,8]. In this manuscript, we consider two elements of the scattering matrix: the intensity, F_{11} and the degree of linear polarization for unpolarized incident light, $-F_{12}/F_{11}$. The measurements are carried out with a HeCd laser ($0.442\,\mu m$, 40 mW) and a HeNe laser (0.633 nm, 5 mW) as light sources. The laser light is scattered by ensembles of randomly oriented particles located in a jet stream produced by an
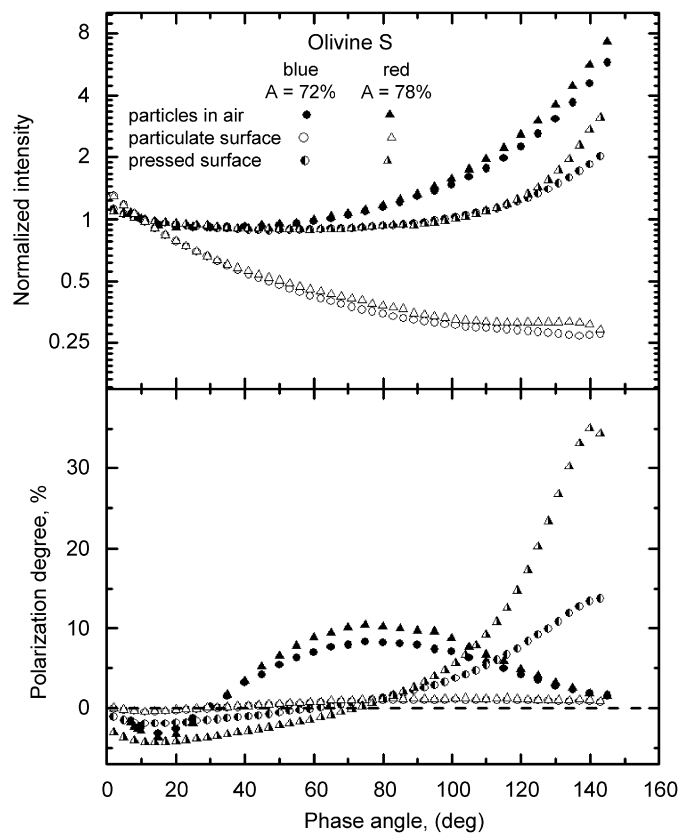

Fig. 3. The same as in Fig. 2 for the olivine S powder.

aerosol generator. The scattered light is detected with a photomultiplier that moves along a circular ring at the center of which the particle stream is located.

We compare the experimentally obtained phase functions and degrees of linear polarization for unpolarized incident light as a function of the phase angle of several powder samples (see Table 1) using these two instruments. The samples have been described and characterized previously [4,5,8]. Moreover, we have obtained detailed photomicrographs of the samples using a scanning electron microscope, e.g. [5].

3. Result of measurements

Results of the sample measurements are presented in Figs. 2–10. All figures present measurements of intensity and polarization degree at the two wavelengths for particles in air and particulate surfaces before and after compression. In the first case, we deal with independent single-particle scattering. The scattering demonstrates strong forward and a relatively small backward increase in intensity. All the compressed samples also reveal prominent forward scattering. The uncompressed samples mainly do not show this feature. This is consistent with the shadow-hiding effect.

As can be seen all the samples demonstrate positive polarization branches with maxima at large phase angles. For bright uncompressed surfaces, the branches are very shallow as compared to those of the aerosol particles. Generally polarization phase dependencies of uncompressed surfaces qualitatively resemble those of single particles, suggesting that for the uncompressed surfaces, the positive polarization is probably dominated by single-particle scattering. Bright particulate surfaces have lower values of the positive polarization maxima because multiple scattering can suppress polarization. The polarization maximum of single-particle scattering
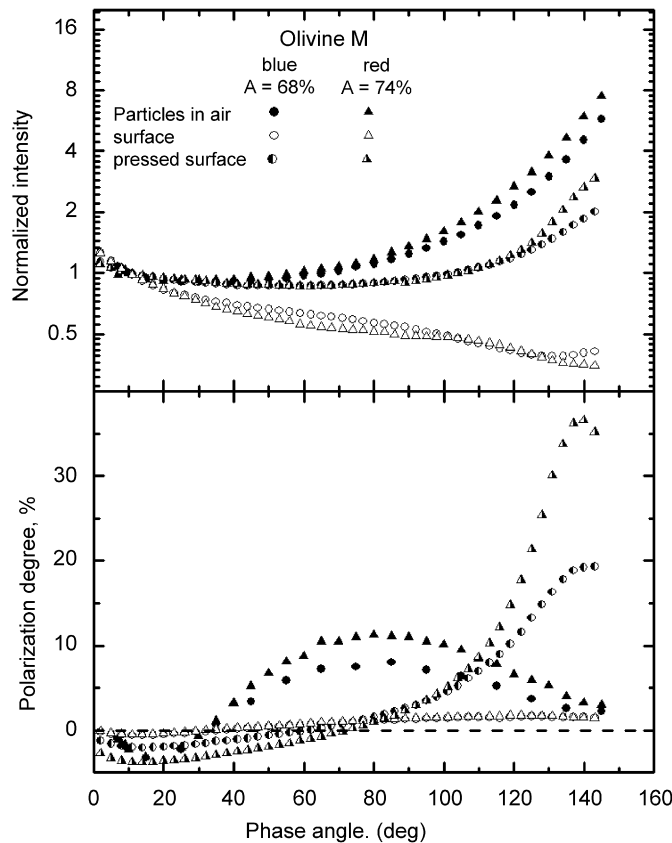

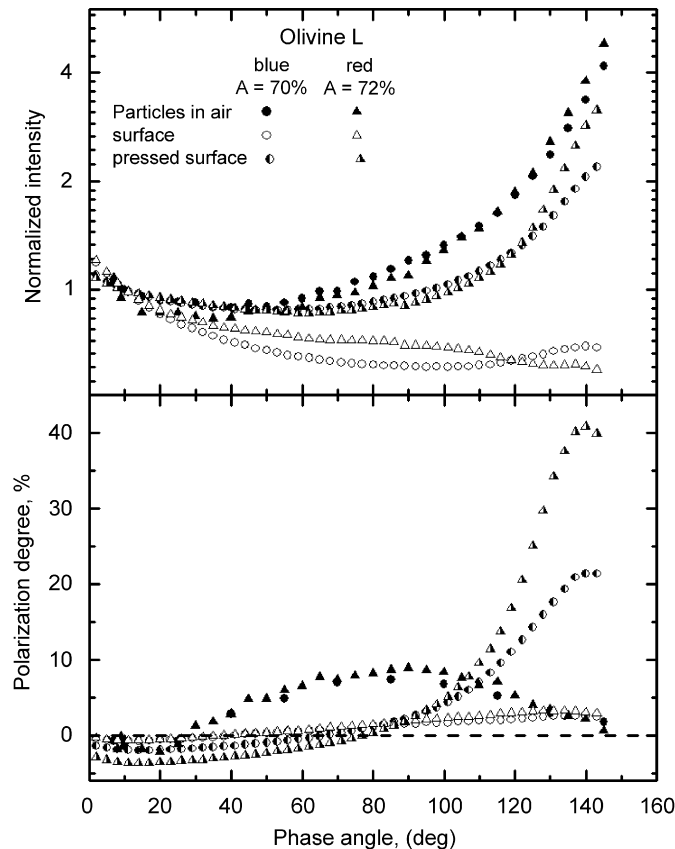Fig. 4. The same as in Fig. 2 for the olivine M powder.

Fig. 5. The same as in Fig. 2 for the olivine L powder.

is located at smaller phase angles than that of the particulate surfaces. This also can be related to multiple scattering in the particulate surfaces. Prominent differences are observed for polarimetric curves of compressed and uncompressed samples. The compression is made with a glass plate, and the sample porosity can decrease by nearly a factor of two, while the sample microtopography becomes much smoother. After compression the polarimetric curves have much more prominent maxima, shifting to larger phase angles. As for increasing maximum values, partially this is due the compression smoothing the topography and suppressing the multiple scattering on the surfaces, which provides a larger contribution from the single-particle scattering. However, for some surfaces the maximum values for the compressed samples can be noticeably higher than those for the aerosol particles, showing that the positive polarization branch is formed not only with the single-particle scattering. At large phase angles, when the incident and emergent angles are near grazing, coherent single scattering can be observed, if electromagnetic phase shifts between rays scattered by different surface particles is small enough. As can be seen in Fig. 11, the larger the phase angle, the smaller the shift, which can provide constructive interference. It can be shown that the condition for constructive interference is $h((1 + \cos \alpha)/\cos i) \ll \lambda$, where h is the height, λ is the wavelength, α and i are the phase angle and angle of incidence, respectively (Fig. 11). When this condition holds, the particulate surfaces appear relatively smooth and scatter light as a nearly plane surface whose reflections are described by the Fresnel formulas that predict high polarization degree for the phase angle range.

All the surfaces also demonstrate a prominent backscattering effect at this observation geometry. The brightness phase curves of the surfaces and aerosol particles almost coincide with each other at small phase angles of less than 20°. Aerosol particles reveal negative polarization branches with a depth of a few percent at small phase angles. Uncompressed particulate surfaces also show negative polarization, however, their depths
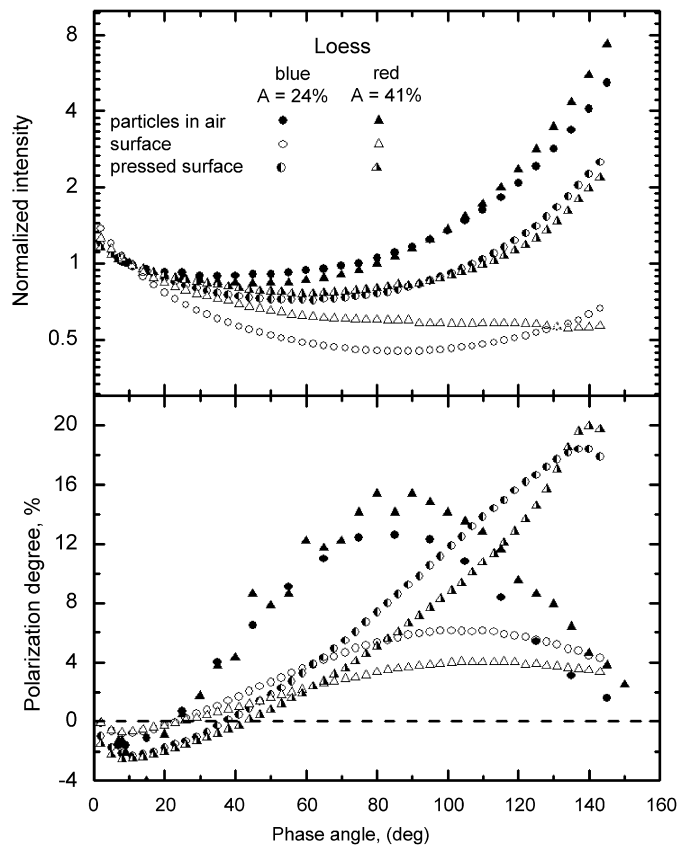
Fig. 6. The same as in Fig. 2 for the loess sample.

are less than those of the aerosol particles (see also [4,5]). Partially this effect is a remnant of the negative polarization of the single scattering by the particles that constitute the surfaces. On the other hand, it can be related to pure geometric factors as the compressed surfaces reveal negative polarization branches deeper and wider at small phase angles than before compression.

There is a simple mechanism that can be responsible for the negative polarization at slanting view. Fig. 12 shows double scattering in the surface plane at tilted geometry. Scatterers 1 and 2 lie in the scattering plane, whereas, scatterers 3 and 4 lie in a plane perpendicular. If we consider small single scatterers whose polarization tends to be positive over the entire phase-angle range, the double scattering events $0 \to 3$ and $0 \to 4$ result in a negative polarization, whereas, the double scattering events $0 \to 1$ and $0 \to 2$ result in positive polarization. Obviously, for large tilts the negative polarization produced by the double scattering events $0 \to 3$ and $0 \to 4$ dominates the positive polarization originated with the double scattering $0 \to 1$ and $0 \to 2$ (when the tilt is close to $90°$ the double scattering $0 \to 1$ and $0 \to 2$ produce almost zero polarization). This interpretation is consistent with the fact that the negative polarization branches are more prominent for compressed (smoothed topography) samples.

4. Theoretical modeling of photometric data

While qualitative explanations of some effects are physically enlightening, they are not a substitute for a quantitative comparison of the experimental data with existing theoretical models of light scattering by particulate surfaces. For this purpose, the radiative transfer theory might be used, e.g. [3]. Radiative transfer theory allows for calculation of all elements of the scattering matrix, thus providing phase curves of intensity and linear polarization degree. Unfortunately, the theory being formally rigorous,
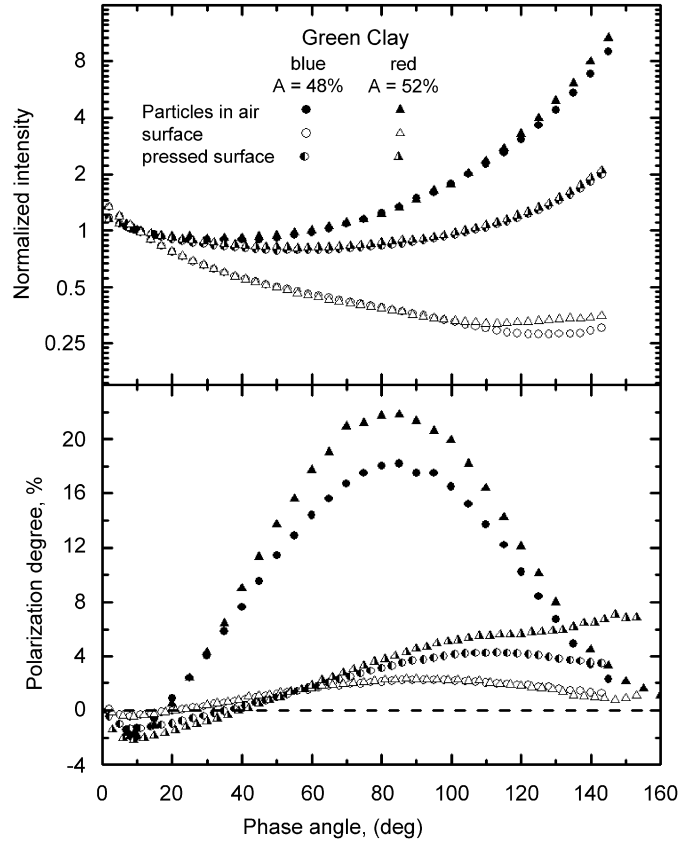
Fig. 7. The same as in Fig. 2 for the green clay powder.

does not take into account the shadow-hiding effect neither between particles in media, nor for particulate surface topography [9]. On the other hand, this effect is the leading factor in optics of particulate surfaces and it cannot be ignored even in the case of bright particulate surfaces (see results presented in Figs. 2–10). For this reason, many workers often prefer to use approximate models, but with accounting for the shadowing effect [2,10,11].

Hapke's model for the bidirectional reflectance distribution function (BRDF) [2] with a later update for anisotropic multiple-scattering approximation [10] is probably the most popular model in use. This model does not consider polarization at all; it only deals with phase dependencies of intensity. The Hapke model involves empirical parameters being considered as proxies for physical properties of the surface. The model [10] takes into account the effect of coherent backscattering enhancement, but here we ignore it, since for fitting we used the photometric data at phase angles larger than $7°$ where this effect almost does not influence results. We present the BRDF formula in the following form:

$$R(\alpha, w, B_0, h, b, c, \theta) = \frac{w}{4\pi} \frac{\mu_{0e}}{(\mu_0 + \mu)}$$
$$\times \left\{ \begin{array}{l} (1 + B(\alpha, B_0, h))P(\alpha, b, c) + \Re(\mu_0, b, c)(H(\mu, w) - 1) \\ + \Re(\mu, b, c)(H(\mu_0, w) - 1) + \rho(b, c)\big[(H(\mu, w) - 1)(H(\mu_0, w) - 1)\big] \end{array} \right\}$$
$$S(\mu_0, \mu, \psi, \theta), \tag{1}$$

where α is the phase angle, μ_0 and μ are cosines of the incident and emergent angles, respectively. ψ is the azimuth angle between planes of incidence and scattering, and w is the single scattering albedo. Adjustable parameters of the model are described below.
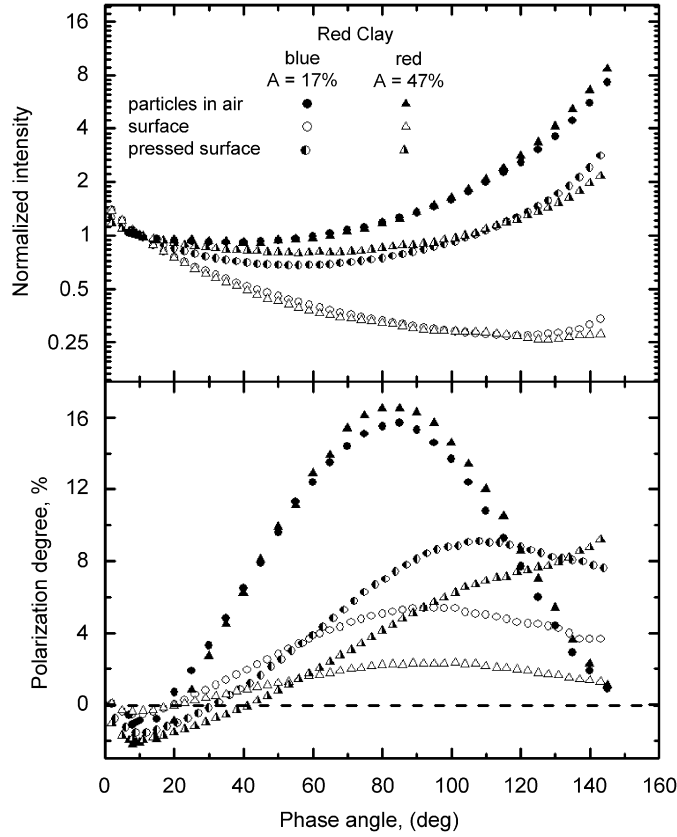
Fig. 8. The same as in Fig. 2 for the red clay powder.

(a) The parameters B_0 and h control the amplitude and angular width of the shadow-hiding opposition effect,

$$B(\alpha, B_0, h) = \frac{B_0}{1 + \left(\tan\left(\alpha/2\right)/h\right)}, \qquad (2)$$

where

$$h = -\tfrac{3}{8} \ln(1 - \xi), \qquad (3)$$

ξ is the porosity, i.e. the number of particles in the volume of one particle, B_0 is the empirical parameter, characterizing the amplitude of the shadow-hiding opposition effect, $0 < B_0 < 1$.

(b) The values b and c are the parameters of the double Henyey–Greenstein scattering indicatrix of single particles. The forward and backward scattering lobes are described by

$$P(\alpha, b, c) = \frac{1+c}{2}\left[\frac{1-b^2}{(1 + 2b\cos\alpha + b^2)^{3/2}}\right] + \frac{1-c}{2}\left[\frac{1-b^2}{(1 - 2b\cos\alpha + b^2)^{3/2}}\right]. \qquad (4)$$

(c) The value $S(\mu_0, \mu, \psi, \theta)$ is the shadow function of surface roughness. Here the parameter θ is supposed to be an estimation of effective roughness of the surface, it is an average topographic slope angle to the global normal of the surface. Roughness alters the local incidence and emergence angles, therefore, if the roughness effect is not negligible then the model deals with effective cosines μ_{0e} and μ_e which are functions of θ, μ_0, μ, and ψ. We do not show here the explicit equations for $S(\mu_0, \mu, \psi, \theta)$, as they are very cumbersome [2].
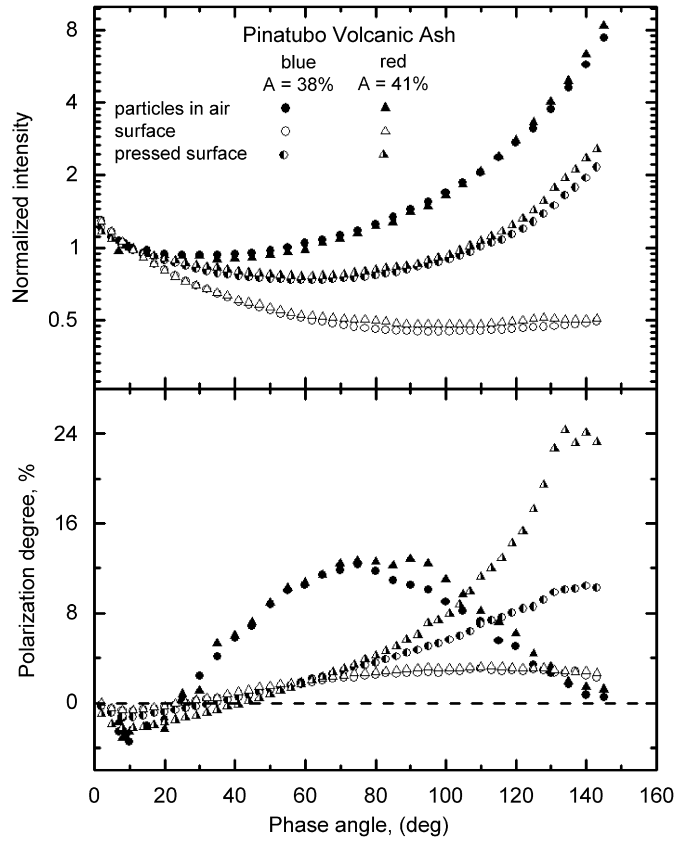
Fig. 9. The same as in Fig. 2 for the Pinatubo volcano ash.

(d) Chandrasekar's *H*-functions represent multiple scattering for isotropic scatterers. An approximate expression for the *H*-function reads as follows [2]:

$$H(x,w) = \left[1 - wx \left\{ \frac{1 - \sqrt{1-w}}{1 + \sqrt{1-w}} + \frac{1 - 2x\left((1-\sqrt{1-w})/(1+\sqrt{1-w})\right)}{2} \ln \frac{1+x}{x} \right\} \right]^{-1}. \tag{5}$$

(e) For anisotropic scatterers with the double Henyey–Greenstein scattering indicatrix the other factors of the multiple scattering term in (1) are [10]

$$\Re(x,b,c) = 1 + \sum_{n=1}^{15} A(n)\beta(n,b,c)Leg(n,x), \tag{6}$$

$$\rho(b,c) = 1 + \sum_{n=1}^{15} A(n)^2 \beta(n,b,c), \tag{7}$$

where

$$A(n) = \begin{cases} 0 & \text{if } n \text{ is even} \\ \frac{-1^{((n+1)/2)}}{n} \frac{1\cdot3\cdot5...n}{2\cdot4\cdot6...(n+1)} & \text{if } n \text{ is odd} \end{cases}, \tag{8}$$

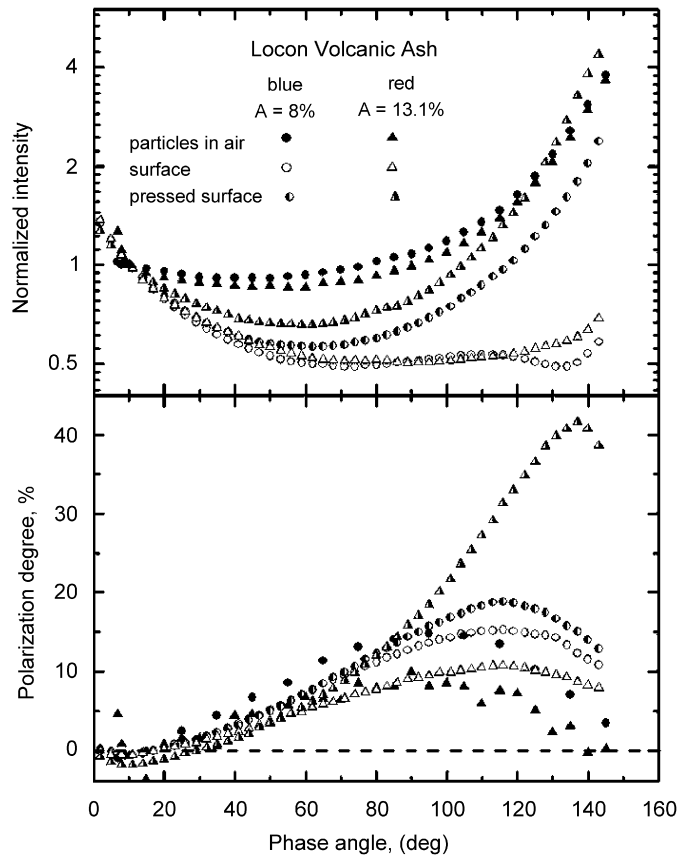$\beta(n,b,c) = c(2n+1)b^n$ and $Leg(n,x)$ are Legendre functions.

Fig. 10. The same as in Fig. 2 for the Lokon volcano ash.

Thus, the Hapke model operates with 6 parameters B_0, h, b, c, w, and θ. In general, these are too many to expect a single-valued fitting. Fortunately the Amsterdam measurements of single-particle scattering functions allow us to find the two parameters b and c of the Henyey–Greenstein scattering indicatrix and then to incorporate them into the model. Table 1 presents values for the parameters calculated using the weighted least-squares fit method. We use the lower weights for points on the phase curves corresponding to large phase angles $>110°$, because we consider the forward-scattering diffraction peak typical for individual particles as being depressed in particulate media. Finally, the quality of the least-squares fitting is better for phase angles $<110°$ than for larger phase angles (see Fig. 13). All samples reveal forward-scattering properties ($c > 0.68$ for $\lambda = 0.44 \, \mu m$ and $c > 0.66$ for $\lambda = 0.63 \, \mu m$) with varying lobe width ($b = 0.28$–0.56).

We use the values of the parameters b and c given in Table 1 in order to fit the Hapke function (1) to the light-scattering measurements of the particulate surfaces. For this, we pave the four-dimensional space of the rest parameters (B_0, h, θ, w) with a grid of 100 points along each axis [12]. We vary B_0, h, and w from 0 to 1 with a 0.01 step and θ from 0 to 50° with a 0.5° step. As a result, for each sample we run 10^5 solutions and calculate for each one the residual mean square (rms) error resulting from the phase curve fit. We rank all solutions according to the rms increase and finally have analyzed the sequence of the 1000 (0.001% of the total number of cases) best fitting solutions. The analysis has prompted us to build up statistics (mean and standard deviation) from the best solutions for deriving Hapke-parameter estimates. In Fig. 14, we present results of the best fits for the 9 samples studied at two wavelengths $\lambda = 0.44 \, \mu m$ (a) and $\lambda = 0.63 \, \mu m$ (b) (c and uc denote compressed and uncompressed samples, respectively). The best fit values are shown with filled circles, average values from 1000 best fits are shown by open circles, and standard deviations for the set of 1000 best values are shown as error bars. These plots immediately point to the problem of uncertainty of best fits. While the
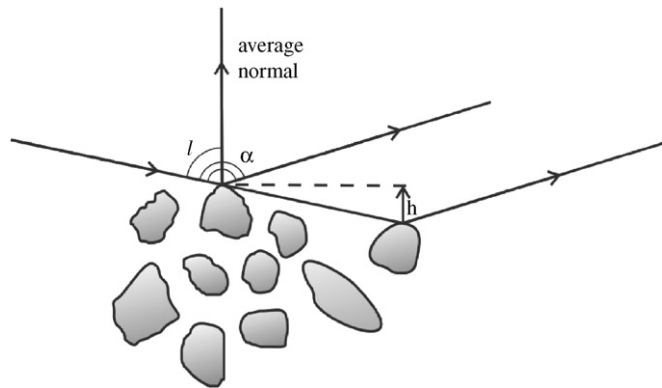
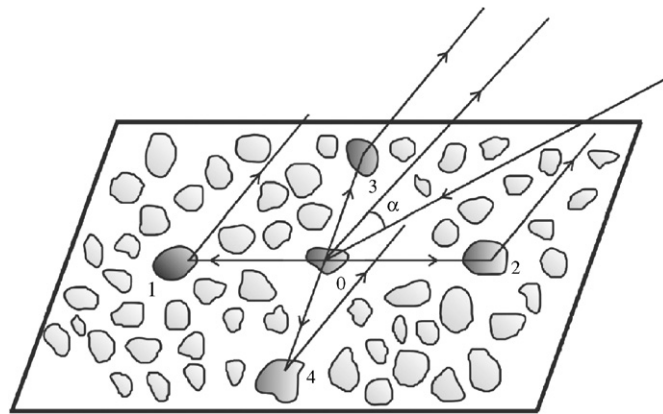Fig. 11. The interference of singly scattered rays at large phase angles.

Fig. 12. Double-scattering mechanism of the negative polarization for tilted particulate surfaces.

parameter w is determined more or less satisfactorily, the parameters B_0 and h (especially) have large dispersions in their best fits. This means that one can "optimally" fit the experimental phase-angle dependencies with many significantly different combinations of the parameters. The parameter h is a function of the volume density of the samples, following formula (3). Unfortunately, we do not see evidence for this in the best fit of the h values when we compare the results from the compressed and uncompressed samples. For the parameter h the samples should be divided into two groups (compressed and uncompressed), however, we observe this neither in blue (Fig. 14a) nor in red (Fig. 14b) light: there is no systematic wavelength dependence of the parameter h.

On the other hand, we find distinct separation of the compressed (c) and uncompressed (uc) samples for the parameter θ. The uncompressed samples are characterized by high values of θ, 20–50°, whereas, the compressed samples show low values usually $<10°$. At least qualitatively, such a difference is in agreement with the laboratory measurements, though the large-scale topography parameter θ is hardly applicable directly to the characterization of the surfaces of our small samples. In some cases, one can see a wavelength dependence on θ, which should not be. The roughness function S, which is affected by θ, significantly changes the BRDF at large phase angles. For θ values $>30°$ the function S can be responsible for a bend feature that results in unsatisfactory quality of fitting for uncompressed samples. Figs. 15 and 16 suggest results of the best fits with the 4 parameters (B_0, h, θ, w), respectively, at $\lambda = 0.44$ and $0.63 \,\mu m$ for the following samples: Locon volcano uc (a), Locon volcano c (b), Pinatubo uc (c), Pinatubo c (d), Olivine S uc (e), Olivine S c (f), Olivine L uc (g), Olivine L c (h), Feldspar uc (i), Feldspar c (j). As can be seen the fits for compressed samples are usually better for the uncompressed ones. At least for compressed samples we had no problem with the bend feature.
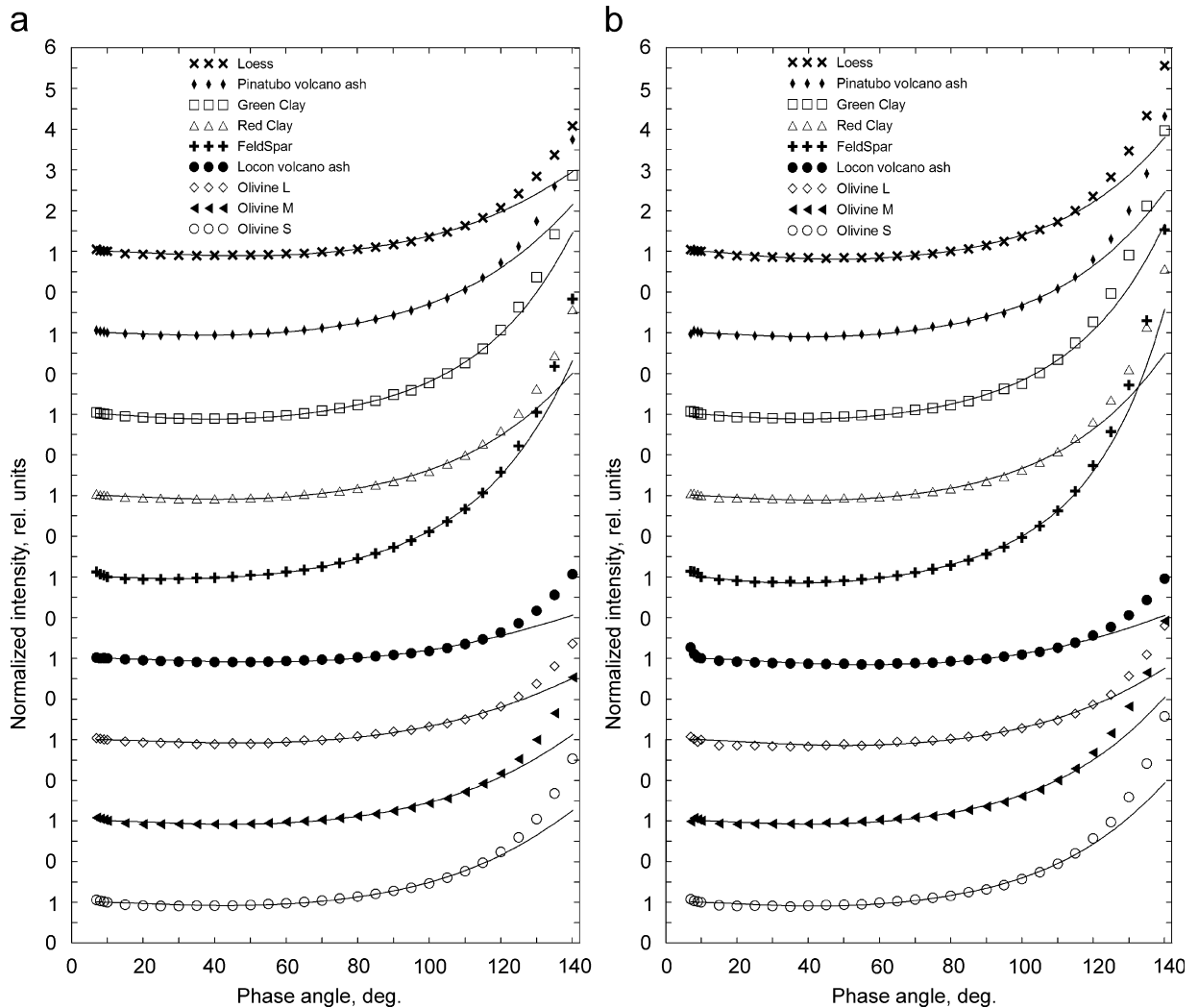
Fig. 13. Fitting results for the photometric phase dependencies of single particles with formula (1). Points are the measurements; the curves are the results of fitting using the parameters from Table 1. (a) and (b) correspond to $\lambda = 0.44$ and $0.63\,\mu m$, respectively.

The values of the single scattering albedo parameter w slightly correlate with the sample albedo. For instance, the dark Locon volcano sample (albedo is 8% in blue and 13% in red light) is characterized by $w < 0.2$; whereas, the bright Olivine M sample (albedo is 68% in blue and 74% in red light) demonstrates $w > 0.8$. On the other hand, there are many exceptions to this tendency. For example, in red light, measurements of the uncompressed Red clay and Green clay samples (albedo 47.3% and 52.2%) show $w \sim 0.3$ and ~ 0.5, but the compressed and uncompressed Loess samples with moderate red albedo $\sim 44\%$ reveal the highest w values ~ 1. According to the Hapke model, the parameter w should not vary for the same sample in different compaction states at all. However, the Green clay, Red clay, Loess, and some other samples do not obey this rule.

Thus we see that the Hapke model describes our laboratory photometric data unsatisfactorily. One could suppose that the model operates with parameters that are closely related to each other resulting in unstable fitting. To check if the three parameters B_0, h, and w can mimic θ variations in the fitting process we exclude θ from the model equation (1) considering $S(\mu_0, \mu, \psi, \theta) \equiv 1$. We again vary the parameters B_0, h, w from 0 to 1 with a 0.01 step and for each sample we run 10^4 solutions. Then we have analyzed the 10 best solutions to form the set of 0.001% of the total number of cases. The plots in Fig. 17 show strong
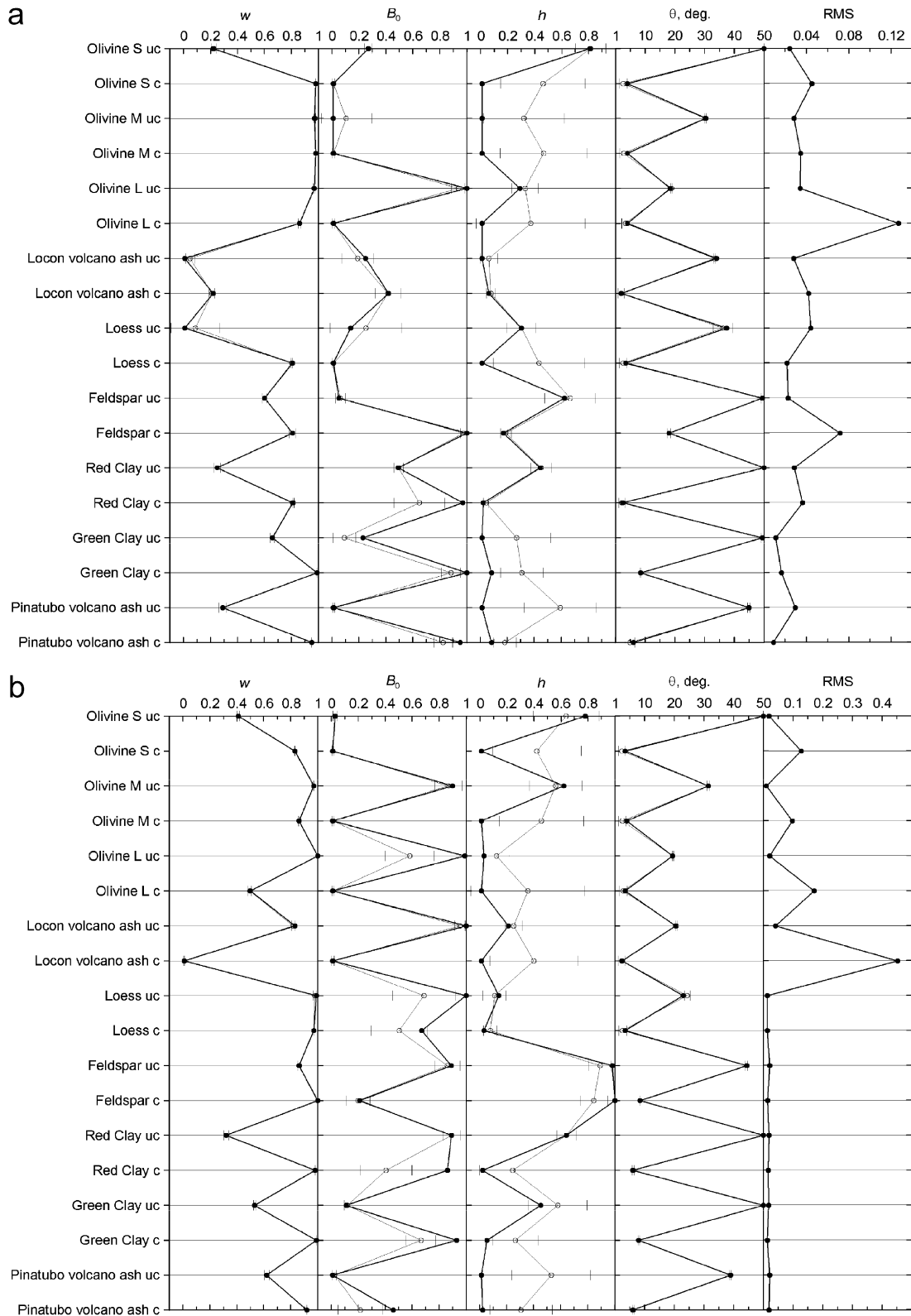
Fig. 14. Results of fitting with the Hapke model [2,10] for 18 samples with the parameters w, B_0, h, and θ (see also estimates of rms). Filled circles correspond to the best fits, open circles correspond to average values for 0.001% of whole set of solutions, error bars represent standard deviations for 0.001% of the whole set of solutions. Panels (a) and (b) present data for $\lambda = 0.44$ and $0.63\,\mu m$, respectively.
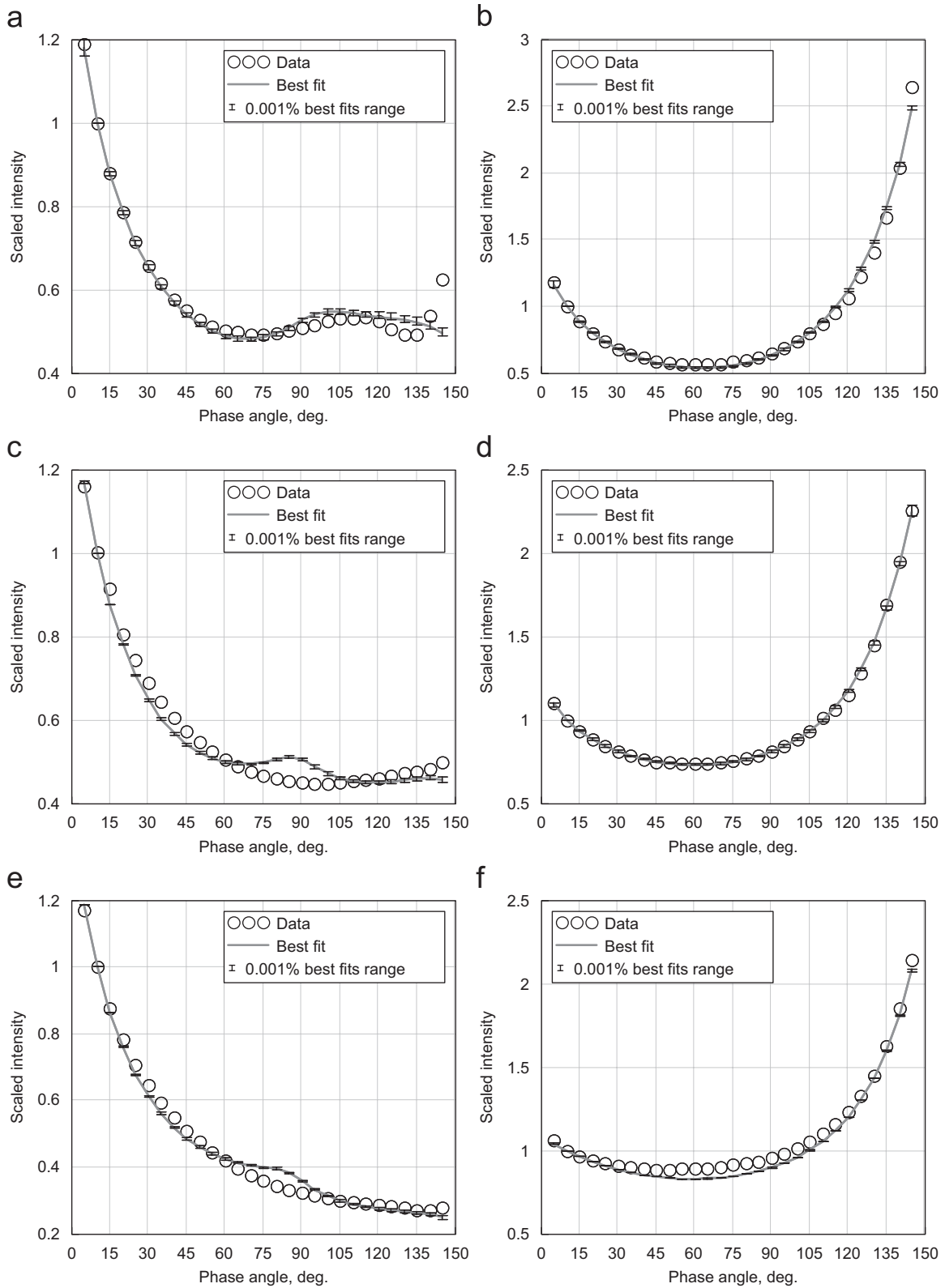
Fig. 15. Examples of the best fits with the 4 parameters at $\lambda = 0.44\,\mu m$ for the following samples: Locon volcano *uc* (a), Locon Volcano *c* (b), Pinatubo *uc* (c), Pinatubo *c* (d), Olivine S *uc* (e), Olivine S *c* (f), Olivine L *uc* (g), Olivine L *c* (h), Feldspar *uc* (i), Feldspar *c* (j).
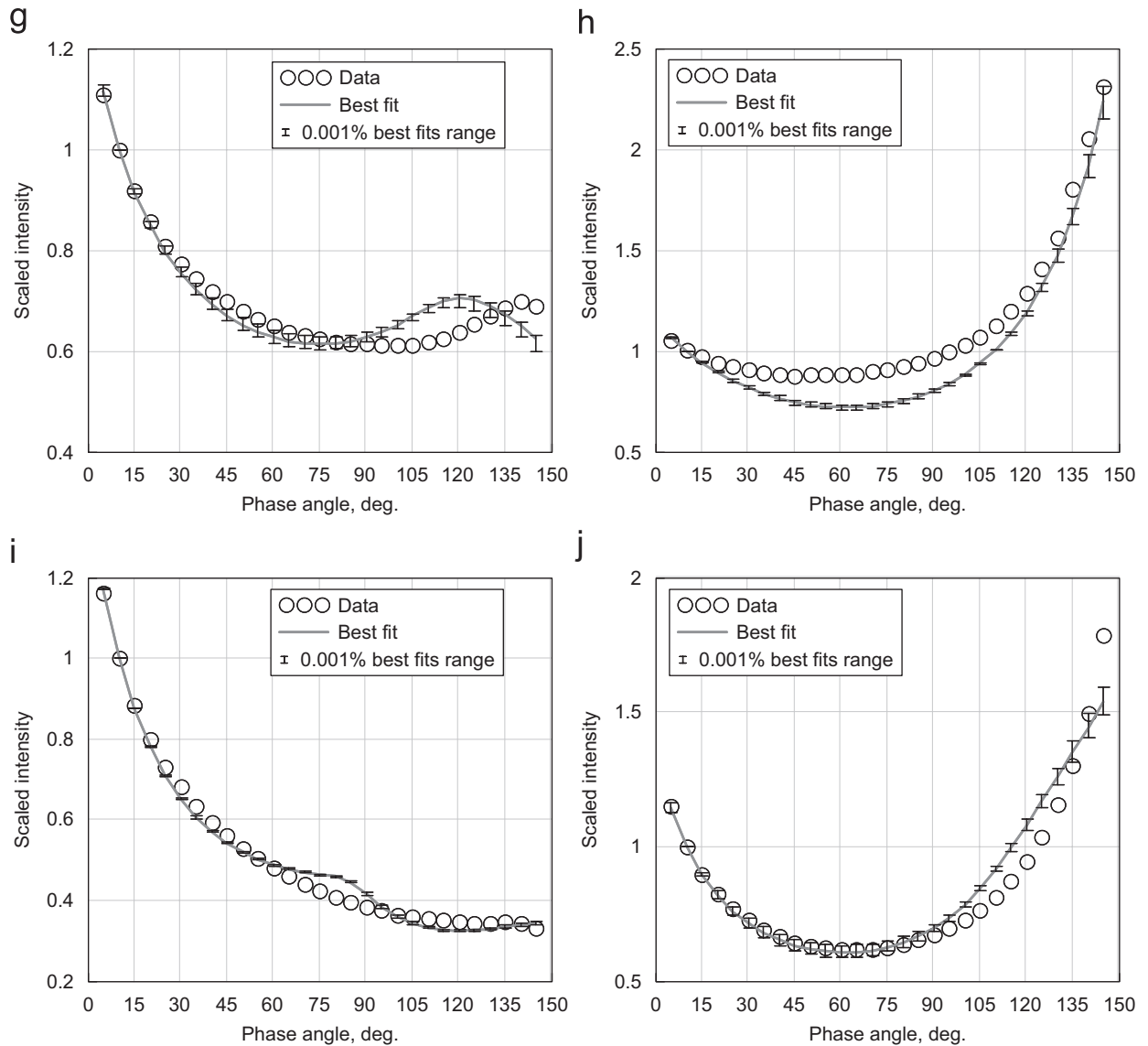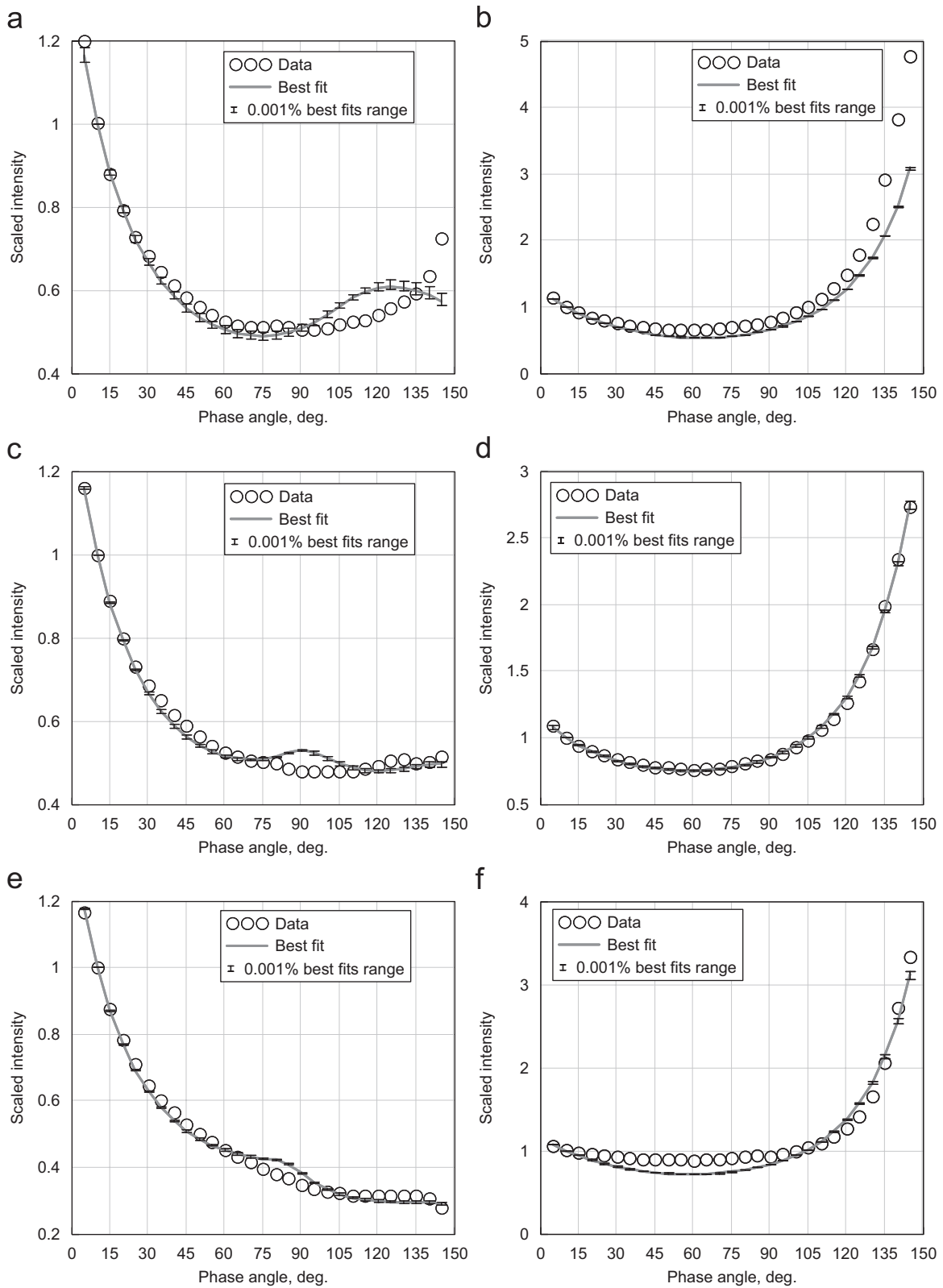
Fig. 15. (*Continued*)

differences for the best fit rms values between compressed and uncompressed samples; the only exclusion is the Locon volcano sample measured in red light: it has an extremely high-amplitude forward-scattering lobe, which leads to an underestimation of the BRDF with the fitting procedure. Photometric curves that were characterized by high θ values in previous modeling cannot be fitted by variations of B_0, h, w. The best fit with the three Hapke parameters for compressed samples remain more or less satisfactory. We present several examples of best fits for 3-parameter modeling in Figs. 18 and 19. We note that we did not find any reliable correlations of the parameters B_0, h, w with albedo of the samples for 3-parameter or 4-parameter modeling. Thus we conclude that the Hapke BRDF model [2,10] applied to laboratory measurements of different particulate samples reveals great uncertainties of the fitting parameters and their values often do not correspond to the actual physical state of the laboratory samples. We also believe that the problem of uncertainties of best fit parameters is an intrinsic property of the Hapke equation (1). We do not observe sharp minima of the rms functions estimated for best fits. This leads to largely unconstrained solutions when

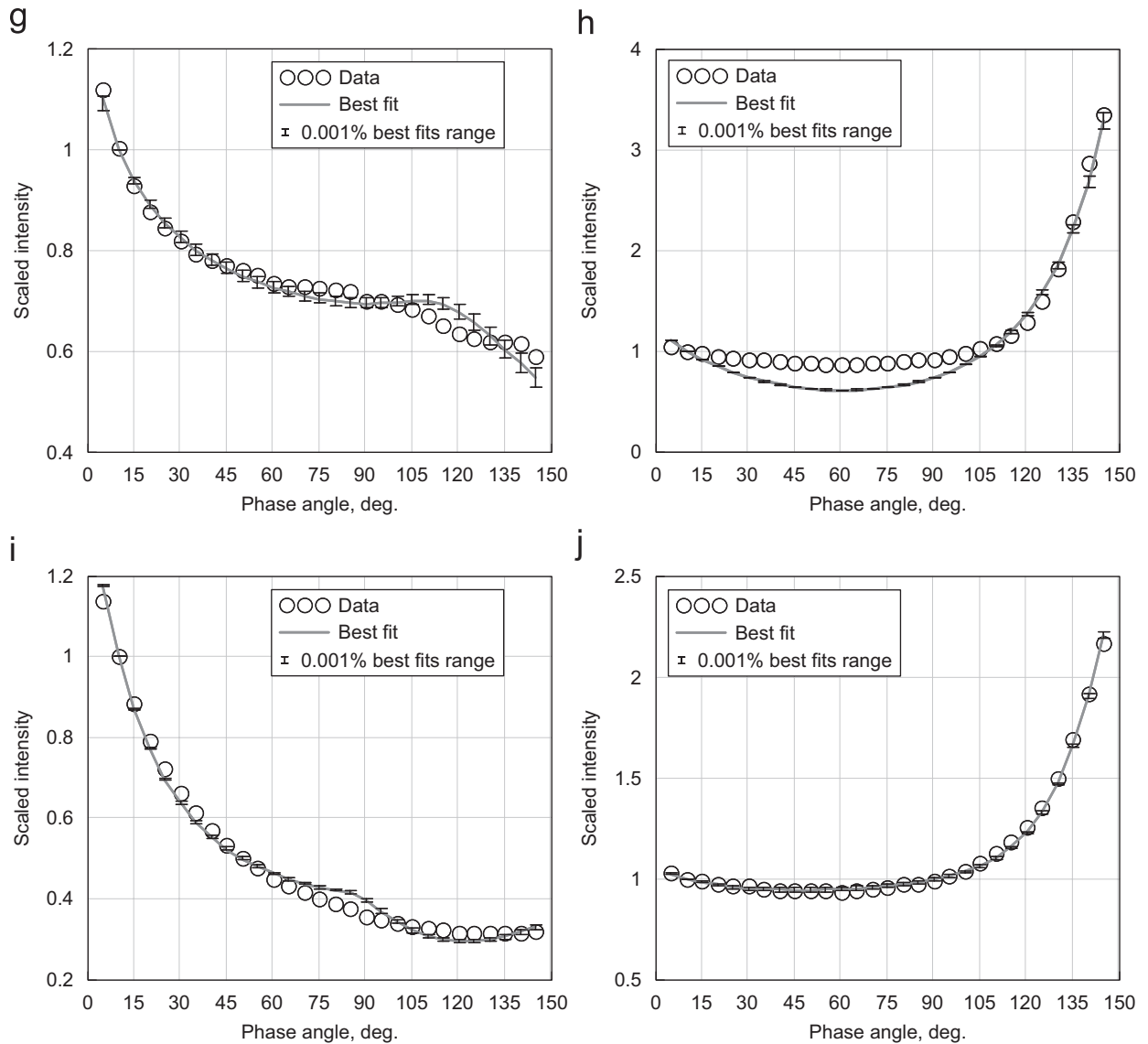Fig. 16. The same as in Fig. 15 for $\lambda = 0.63\,\mu m$.

Fig. 16. (*Continued*)

photometric parameters varying in a wide range fit the experimental data with fair accuracy at the level of the data noise.

5. Conclusion

Photometric and polarimetric laboratory measurements of particulate surfaces with different compression and aerosol particles at the large-phase-angle range from 7 to 150° were carried out in blue and red light ($\lambda = 0.44$ and $0.63\,\mu\mathrm{m}$) with two different instruments: Kharkov's large-phase-angle photopolarimeter (for surfaces) and Amsterdam's polar nephelometer (for aerosol particles). The measurements of particulate surfaces were made at a constant viewing angle equal to 70°. We note the main results:

1. The results suggest that the positive polarization maximum, which is observed for particulate surfaces at large phase angles, is formed mainly due to contribution of single-particle scattering. This polarization is
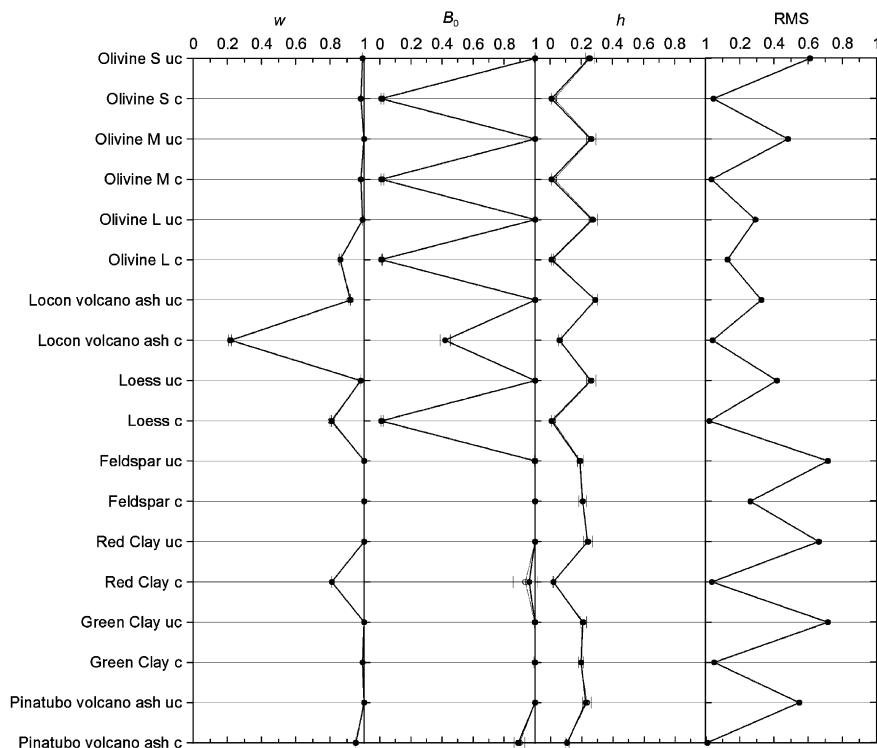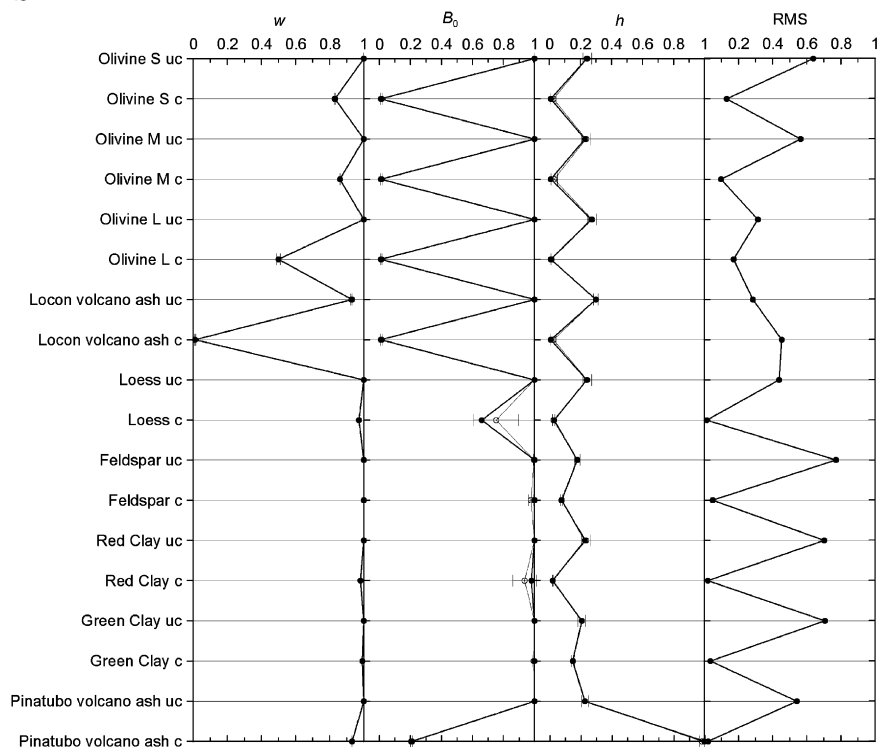
Fig. 17. Results of direct Hapke modeling for 18 samples with the three parameters w, B_0, and h (estimates of rms are also given). Filled circles correspond to the best fits, open circles correspond to average values for 0.001% of whole set of solutions, error bars represent standard deviations for 0.001% of the whole set of solutions. Panels (a) and (b) present data for $\lambda = 0.44$ and 0.63 μm, respectively.
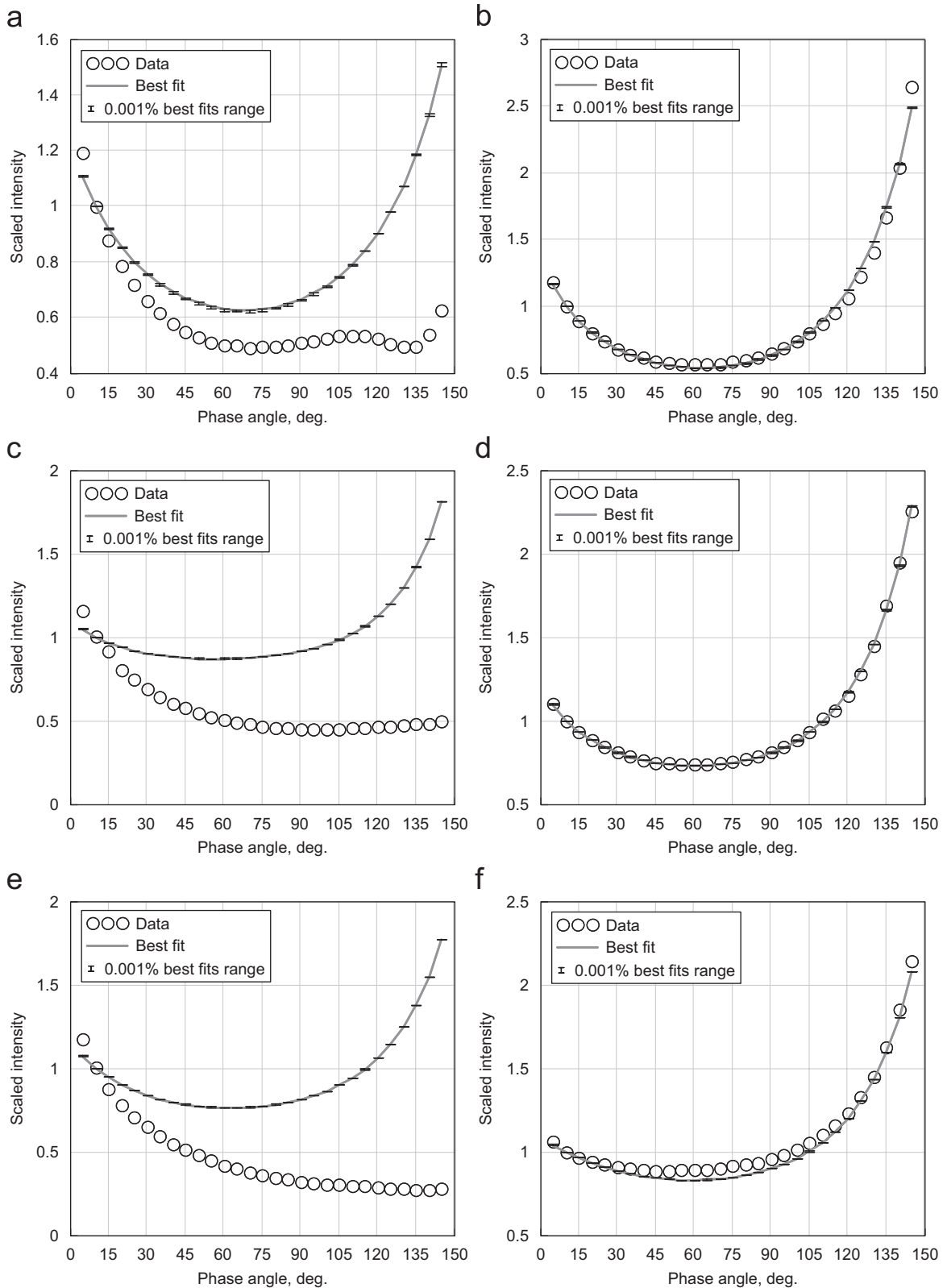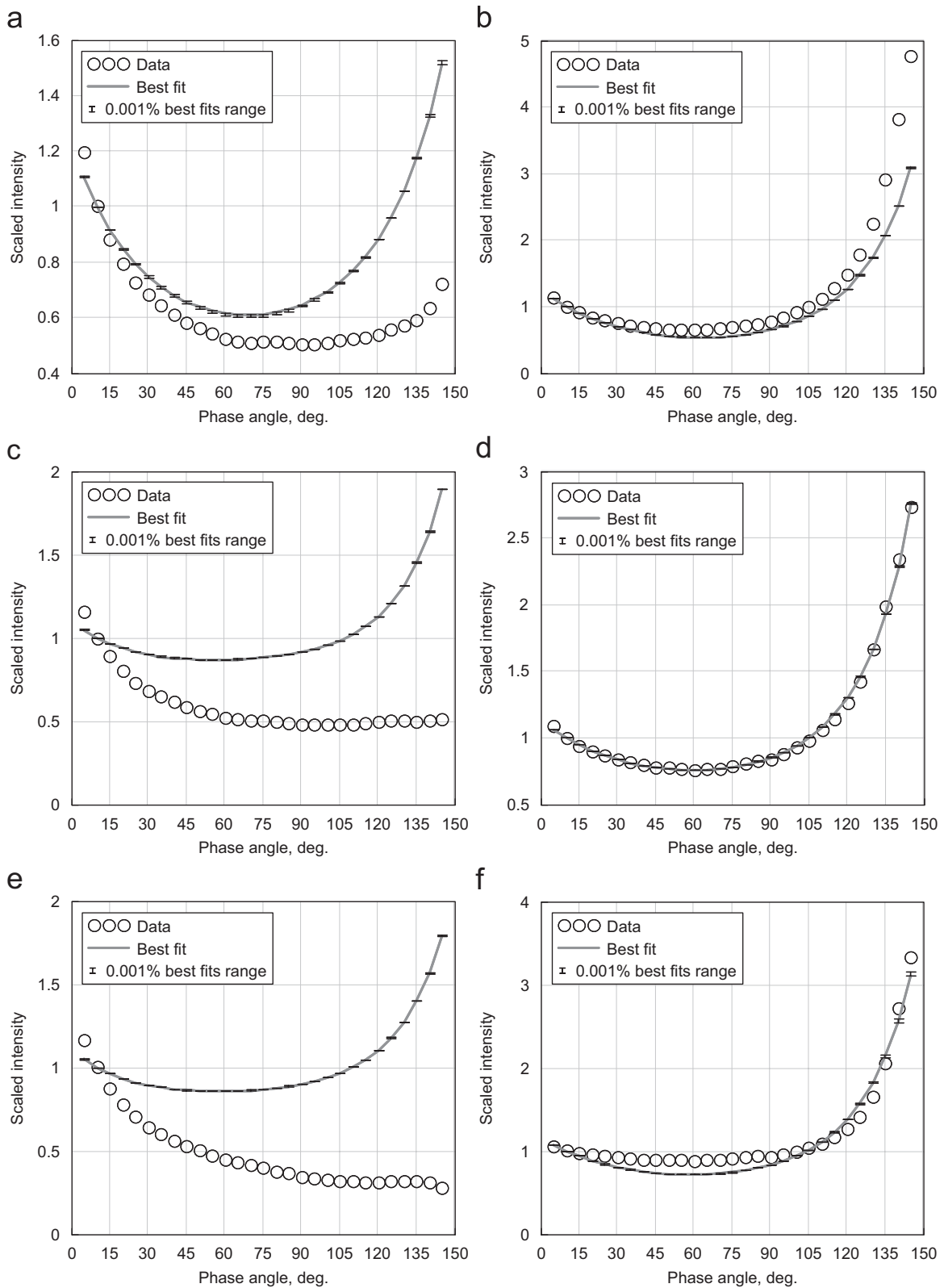
Fig. 18. Examples of best fits with the 3 parameters at $\lambda = 0.44\,\mu m$ for several samples: Locon volcano *uc* (a), Locon vcolcano *c* (b), Pinatubo *uc* (c), Pinatubo *c* (d), Olivine S *uc* (e), and Olivine S *c* (f).

Fig. 19. The same as in Fig. 15 for $\lambda = 0.63\,\mu m$.

suppressed in particulate surfaces by multiple scattering. We observe an increase of polarization degree at large phase angles with increased sample compression. This effect perhaps is due to the constructive interference of singly scattered rays at their grazing incident and emerging propagation.
2. We have found negative polarization at small phase angles, which is sharply strengthened when the sample is compressed. Partially this is a geometric effect at slanting view, which is explained with double scattering.
3. Comparison of measured photometric phase-angle dependencies with those of the Hapke photometric model reveals several shortcomings of the model. The main of them is spectral dependence of model parameters that should be independent of wavelength.

Acknowledgment

References

[1] Shkuratov Y, Opanasenko NV. Polarimetric and photometric properties of the moon: telescope observation and laboratory simulation. 2. The positive polarization. Icarus 1992;99:468–84.
[2] Hapke B. Theory of reflectance and emittance spectroscopy. Cambridge University Press; 1993 450pp.
[3] Mishchenko M, Dlugach J, Yanovitskij E, Zakharova N. Bidirectional reflectance of flat, optically thick particulate layers: an efficient radiative transfer solution and applications to snow and soil surface. JQSRT 1999;63:409–32.
[4] Shkuratov Y, Ovcharenko A, Zubko E, Volten H, Muños O, Videen G. The negative polarization of light scattered from particulate surfaces and of independently scattering particles. JQSRT 2004;88:267–84.
[5] Shkuratov Y, Bondarenko S, Ovcharenko A, Pieters C, Hiroi T, Volten H, et al. Comparative studies of the reflectance and degree of linear polarization of particulate surfaces and independently scattering particles. JQSRT 2006;100:340–58.
[6] Weidner V, Hsia J. Reflection properties of pressed polytetrafluoroethylene powder. J Opt Soc Am 1981;71:856–61.
[7] Muñoz O, Volten H, de Haan J, Vassen W, Hovenier J. Experimental determination of scattering matrices of olivine and Allende meteorite particles. Astron Astrophys 2000;360:777–88.
[8] Volten H, Muñoz O, Rol E, de Haan J, Vassen W, Hovenier J, et al. Scattering matrices of mineral aerosol particles at 441.6 and 632.8 nm. J Geophys Res 2001;106:17375–401.
[9] Shkuratov YuG, Stankevich DG, Petrov DV, Pinet PC, Cord Au, Daydou YH. Interpreting photometry of regolith-like surfaces with different topographies: shadowing and multiple scatter. Icarus 2005;173:3–15.
[10] Hapke B. Bidirectional reflectance spectroscopy. 5. Coherent backscatter opposition effect and anisotropic scattering. Icarus 2002;157:523–34.
[11] Lumme K, Bowell E. Radiative transfer in the surfaces of atmosphereless bodies. I. Theory. Astron J 1981;86:1694–704.
[12] Kaydash VG, Pinet PC, Baratoux D, Besse S, Jehl A, Chevrel S. Lunar photometry from Clementine multiangular data: analysis of Hapke parameters estimate and implication for upcoming smart-1 spot-pointing data. Lunar and planetary science conf. 37th. LPI Houston. 2006: abstract # 1692.